Local structure and order-disorder transitions in 'empty' ferroelectric tetragonal tungsten bronzes

Jason A. McNulty,[1] David Pesquera,[2] Jonathan Gardner,[1] Andrei Rotaru,[2,3,4] Helen Y. Playford,[5] Matthew G. Tucker,[5,6] Michael A. Carpenter[2] and Finlay D. Morrison[1,]*

[1]EaStCHEM School of Chemistry, University of St Andrews, North Haugh, St Andrews, KY16 9ST, United Kingdom
[2]Department of Earth Sciences, University of Cambridge, Downing Street, Cambridge CB2 3EQ, United Kingdom
[3]University of Craiova, Department of Biology and Environmental Engineering, Str. A.I. Cuza, Nr. 13, Craiova, 200585, Romania
[4]Institute of Physical Chemistry "Ilie Murgulescu" of the Romanian Academy, Department of Chemical Thermodynamics, Str. Splaiul Independentei, Nr. 202, Bucharest, 060021, Romania
[5]ISIS Facility, Rutherford Appleton Laboratory, Chilton, Didcot, OX11 0QX, United Kingdom
[6]Neutron Scattering Division, Oak Ridge National Laboratory, Oak Ridge, Tennessee 37831-6475, United States

Abstract

The 'empty' tetragonal tungsten bronze $Ba_4La_{0.67}\square_{1.33}Nb_{10}O_{30}$ displays both relaxor-like and normal dielectric anomalies as a function of temperature; the former is associated with loss of ferroelectricity and was proposed to originate from anion disordering [*Chem. Mater.,* 2016, **28**, 4616-4627]. Here we present total neutron scattering and pair distribution function (PDF) analysis which shows an increase in the distribution of oxygen-oxygen distances at the relaxor transition and which supports the proposed anion disordering mechanism. The disordering process can be destabilised by reducing the average A-cation size (*i.e.* Nd-doping: $Ba_4(La_{1-x}Nd_x)_{0.67}Nb_{10}O_{30}$); this introduces a more strongly propagating tilt system in line with the previously reported crystal-chemical framework model [*Chem. Mater.,* 2015, **27**, 3250-3261]. Mechanical loss data obtained using resonant ultrasound spectroscopy also indicate destabilisation of the disordering process with increasing Nd-substitution.

Introduction

After perovskites, tetragonal tungsten bronzes (TTBs) are one of the largest structural families of ferroelectrics. The TTB structure consists of a corner-sharing network of BO_6 octahedra which form three cation sites in the channels between the octahedra[1]. In most ferroelectric oxide TTBs only two of these cation sites, the perovskite-like A1-site and the larger A2-site, are occupied and resulting compositions are termed "filled" TTBs. The resulting aristotype unit cell, possessing 4/*mmm* symmetry, therefore has the general formula $A1_2A2_4B1_2B2_8O_{30}$, although A-site vacancies may be present. Distortion of this TTB aristotype is common due to octahedral tilting to relieve A-site-generated strain and results in superstructures and incommensurate modulations[2-5]. In TTBs these, often subtle, structural modifications influence whether ferroelectric (FE) or relaxor-ferroelectric (RFE) behaviour is observed.

Despite its discovery in the 1950s the nature of relaxor behaviour in ferroelectrics continues to be a topic of widespread study. In perovskite materials, relaxor behaviour is often associated with cation disorder: this effect is typified by $Pb(Sc_{0.5}Ta_{0.5})O_3$ which is a 'normal' ferroelectric when the Sc and Ta are ordered at the B-site, but a relaxor when they are disordered[6], while in the archetypal relaxor $Pb(Mg_{1/3}Nb_{2/3})O_3$ (PMN) preservation of local electroneutrality limits ordering of Mg^{2+} and Nb^{5+} generating polar nanoregions in a non-polar matrix giving rise to chemical inhomogeneity and relaxor behaviour[7, 8]. More recently mesoscale structural variations (in the form of octahedral tilting and distortions) have been identified as the origin of relaxor behaviour in perovskites such as $Na_{0.5}Bi_{0.5}TiO_3$ (NBT) and related systems[9-14].

Initially a simple cation-disorder picture was also proposed as the origin of relaxor behaviour for TTBs such as $(Sr,Ba)Nb_2O_6$ (SBN)[15, 16]. However, an early study by Bursill and Lin[5] proposed that the incommensurate structure in SBN arose due to partial ordering between two structural subunits - this provided an early suggestion as to the true origin of relaxor behaviour in TTBs and it is now widely accepted that structural disorder (often giving rise to incommensurations) rather than local cation disorder determine relaxor vs normal ferroelectric behaviour in TTBs. In this regard, understanding of relaxor behaviour in perovskites and TTBs is now reconverging on the need for insights of disorder on varying length-scales, from local (cation) disorder, to mesoscale and long range structural variations.

The nature of the polar ordering (i.e. normal vs relaxor behaviour) in the filled TTB system, $Ba_4R_2Ti_4Nb_6O_{30}$ (R = La^{3+}, Bi^{3+}, Nd^{3+}, Sm^{3+} and Gd^{3+}) had been linked to particular structural changes by Stennett and co-workers.[17-21] In these compositions, the R^{3+} cation fully (and solely) occupies the A1-site while Ba^{2+} is confined to the larger A2-site. When the R cation is comparatively small (Nd^{3+} or smaller), the TTB displays normal ferroelectric behaviour with a commensurate $\sqrt{2}a_0 \times \sqrt{2}b_0 \times 2c_0$ superstructure (where $a_0 = b_0$, c_0 represent the aristotype TTB cell parameters), space group $Ima2$; larger cations (La^{3+} or Bi^{3+}) produce a relaxor response and an incommensurate structure which may be approximated with a $\sqrt{2}a_0 \times 2\sqrt{2}b_0 \times 2c_0$ unit cell, space group $Ama2$.[20] These observations were developed into a crystal-chemical framework model[22] which predicts the nature of the structural modulations and polar ordering, *i.e.*, whether ferroelectric or relaxor behaviour is observed. The resulting properties are a balance of two competing forces which favour normal ferroelectric behaviour: the average A-site size, (A1+A2)/2 which facilitates B-cation displacements along the polar *c*-axis when the A-cations are large; and the tolerance factor, t_{A1}, of the perovskite-like A1-site which determines the degree of octahedral tilting and where low values of t_{A1} result in commensurately modulated tilting. In instances where neither parameter dominates, (frustrated) incommensurate tilting and relaxor behaviour ensues.

The relaxor to ferroelectric crossover has been studied in a number of other TTB systems attributing the origin of the behaviour to the average cation size within the A-sites[23-25] or the anionic sublattice.[26, 27] These studies all identify the disruption of long range structural order, specifically incommensurate tilt modulations[20, 22, 26] or anion disordering as observed in commensurate $Ba_4R_{0.67}Nb_{10}O_{30}$ 'empty' TTBs,[28] as the driver for the onset of relaxor behaviour.

In the latter 'empty' TTB materials, the A1 site is only 1/3 occupied with composition $Ba_4R_{0.67}\;_{1.33}Nb_{10}O_{30}$ (where R = La, Nd, Sm Gd, Dy, and Y). These display a similar A-cation size dependence to that observed in the previously reported filled TTBs ($Ba_4R_2Ti_4Nb_6O_{30}$), with normal ferroelectric behaviour being observed for R = Nd and smaller, while in contrast R = La is a relaxor ferroelectric.[29] The presence of significant (67%) A-site vacancies (hence the term 'empty'[22, 28, 30]) in these systems, however, appears to introduce further complexity with regard to structural modulations and order-disorder, particularly when R = La. The crossover from relaxor to 'normal' ferroelectric behaviour was examined in more detail via the solid solution $Ba_4(La_{1-x}Nd_x)_{0.67}Nb_{10}O_{30}$.[28] La-rich compounds display an additional feature of electrical field-driven

ordering in the temperature regime between the RFE and paraelectric states, (demonstrated by 'pinched' polarisation-electric field (*P-E*) loops, Figure 1), which corresponds to a disordered superstructure[28]. The stability of this disordered regime has a clear thermal and electric field dependence and may be controlled by the average A-cation size (*i.e.*, the ratio of La:Nd)[28].
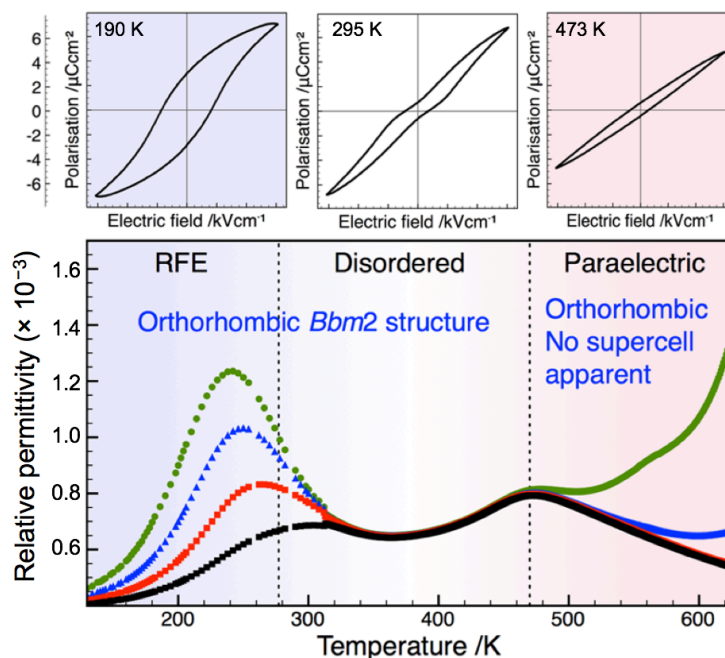
Figure 1. Evolution of relative permittivity, structure and polarisation-electric field (*P-E*) response with temperature for the 'empty' TTB $Ba_4La_{0.67}Nb_{10}O_{30}$[28]. Dielectric data were obtained at 1 kHz (green circles), 10 kHz (blue triangles), 100 kHz (red squares) and 1 MHz (black squares). Hysteresis data were collected at 10 Hz with E_{max} of $\pm$ 60 kVcm^{-1}.

Specifically, the composition $Ba_4La_{0.67}Nb_{10}O_{30}$ exhibits both frequency dependent, relaxor-type (*ca.* 260 K) and frequency independent (*ca.* 480 K) peaks in the dielectric data. Heating through the relaxor-like peak is associated both with the loss of ferroelectric switching and onset of a pinching of the P-E response; both synchrotron X-ray and neutron powder diffraction suggest no change in average symmetry although a change in the thermal expansion is evident. In addition, diffuse scattering in selected area electron diffraction (SAED) indicates that in the temperature region where pinched P-E loops are observed, disorder exists[28]. This structural disorder disrupts long range polar ordering and accounts for the observed loss of ferroelectricity. Application of an electric field reintroduces a large non-linear polarisation of a similar magnitude as in the ferroelectric phase, but on removal of the field non-linear depolarisation signifies a

"backswitching" event associated with the structural relaxation to the disordered phase. This backswitching event occurs against an increasingly large electric field with increasing temperature indicating increased stability of the disorder with increasing thermal energy. Similar pinched loops in $Ba_4Sm_2Ti_4Nb_6O_{30}$ and $Ba_4Eu_2Ti_4Nb_6O_{30}$ filled TTBs[31] (and later in $Ba_4Sm_2Fe_{0.5}Ti_3Nb_{6.5}O_{30}$)[32] have recently been shown to coincide with a field driven incommensurate to commensurate transition using in-situ electron diffraction. It is important to re-emphasise that $Ba_4La_{0.67}Nb_{10}O_{30}$ is commensurate in the temperature range where pinched P-E loops are observed[28].

The temperature range over which the disordered phase and pinched P-E loops persist in $Ba_4(La_{1-x}Nd_x)_{0.67}Nb_{10}O_{30}$ can be reduced by replacement of La with smaller Nd cations at the A1-site. Based on the crystal-chemical framework model, with increasing x, the tolerance factor of the perovskite unit decreases with concomitant increase in degree of NbO_6 octahedral tilting. Greater degrees of tilting in turn facilitates long range propagation of a modulated tilt pattern in the *ab* plane and favours 'normal' ferroelectric properties. As a result, the temperature range over which pinched P-E behaviour is observed decreases: for $x = 1$ ($Ba_4Nd_{0.67}Nb_{10}O_{30}$) a weakly frequency dependent permittivity peak and change from ferroelectric hysteresis to linear P-E behaviour, indicating a normal ferroelectric to paraelectric transition. Although pinched P-E loops in perovskites have been attributed to arise from antiferroelectric states, field-driven structural transitions at temperatures close to phase transitions and extrinsic defects (*e.g.*, defect dipole pairs) these were excluded due to thermal history and electric field cycling experiments (see Ref [33] for more details). As discussed above, the loss of ferroelectric hysteresis in $Ba_4(La_{1-x}Nd_x)_{0.67}Nb_{10}O_{30}$ was attributed to disordering of the anion positions in the *ab* plane based on SAED observations.

In this study we investigate in more detail the structural origin and temperature dependence of the RFE to polar (but non-ferroelectric) transitions in these 'empty' TTBs using total (neutron) scattering methods, supported by resonant ultrasound spectroscopy (RUS) measurements. The data support our initial hypothesis that such behaviour originates from an anion order-disorder transition.[28] While this observation is consistent with the crystal-chemical model for TTBs[22] it is an example of a commensurate TTB relaxor composition. In the wider context of relaxor materials it further emphasises the need for complimentary techniques to understand structure on varying length scales due to the sensitivity of ferroelectric and dielectric properties to disorder.

Experimental Methods

Samples with composition $Ba_4(La_{1-x}Nd_x)_{0.67}Nb_{10}O_{30}$ (x = 0, 0.25, 0.5, 0.75, and 1), were synthesised using a standard solid-state method as described previously.[28] Polycrystalline ceramic pellets (> 95% of theoretical density) were used for dielectric and resonant ultrasound spectroscopy (RUS) measurements. Finely ground powder produced from crushed pellets prepared under the same conditions as for electrical and resonant ultrasound characterisation was used for neutron diffraction structural studies; the powder used for neutron diffraction was the same as used in our previous study where data were collected on heating between 50 and 600 K.

Agilent 4294A and Wayne Kerr 6500B impedance analysers were used for dielectric measurements which were performed between 40 K and 800 K with the sample mounted in a closed-cycle refrigerator and bench top furnace.

Diffraction data for pair-distribution function (PDF) analysis was collected using the Polaris neutron diffractometer at ISIS. A powdered sample (approximately 4.5 g) was loaded into a sealed cylindrical vanadium can. Data was collected on heating between 50 to 600 K and scans recorded for between 1 to 8 hours. Rietveld refinements were carried out using the General Structure Analysis System (GSAS) software package.[34] A 12-term Chebyschev background function was used to account for background coefficients. Parameters refined were lattice parameters, atomic positions, isotropic atomic thermal displacement parameters, appropriate diffractometer constants and profile coefficients. Small peaks from the vanadium can were identified in all diffraction patterns; these were not included in the refinements. The raw diffraction data were corrected onto an absolute scale and Fourier transformed to produce the PDF data using the Gudrun programme covering a wave-vector, Q, up to Q_{max} of 30 Å^{-1} (see supplementary information, SI, for more details). PDF analysis was carried out using the PDFgui software[35] using Q_{broad} and Q_{damp} terms of 0.0228 and 0.0223, respectively, which were determined from refinements to data from a silicon standard (NIST SRM 640b). Partial PDFs were determined from Reverse Monte Carlo (RMC) fitting of PDF data at 50 K using RMCProfile software[36] using a pseudocubic box containing 2858 atoms which was based on a $1 \times 2 \times 4$ supercell of the $Bbm2$ structure as determined from Rietveld refinements. The A-site vacancies were generated at random and no site swapping was allowed (a minimum distance of 1 Å was applied); no other constraints were applied. Maximum move

distances of 0.05 and 0.1 Å were used for cations and anions, respectively, and 43154 moves were accepted out of 96239 attempts.

For Resonant Ultrasound Spectroscopy (RUS) experiments, $Ba_4(La_{1-x}Nd_x)_{0.67}Nb_{10}O_{30}$ pellets were cut in the shape of rectangular parallelepipeds with millimetre size dimensions using a fine (~300 μm) annular diamond saw lubricated with paraffin. Low-temperature RUS measurements were performed by resting the sample between a pair of PZT transducers in a sample holder described by Ref [37], inserted into an Orange helium-flow cryostat. For high-temperature RUS measurements the samples were held between the ends of two alumina rods inserted into a Netzsch 1600 °C furnace, with the driving and pick-up transducers attached to the other end of the rods, outside the furnace, as described in Ref [38]. Spectra were collected either in cooling or heating sweeps, containing 65000 data points between 10 kHz and 1.5 MHz, using dynamic resonance system (DRS) Modulus II electronics and Stanford electronics[39] for low and high temperature measurements, respectively. RUS peak frequencies, f, and widths at half height, Δf, of selected resonance peaks were determined by fitting to an asymmetric Lorentzian profile. The elastic constants which determine each resonant mode scale with f^2, and $\Delta f/f$ is a measure of acoustic attenuation, which is taken here to represent the inverse mechanical quality factor, Q^{-1}. The temperature dependence of f^2 provides a good representation of the evolution of the shear modulus, which is the main contribution to the resonance modes.

Results and Discussion

Dielectric Spectroscopy

Dielectric data for $Ba_4(La_{1-x}Nd_x)_{0.67}Nb_{10}O_{30}$ all display both a low temperature relaxor-like response (*e.g.* for $x = 0$, $T_m = 293$ K for 1 MHz) and a second diffuse, but frequency independent, peak in the relative permittivity at higher temperature ($T^* = 473$ K for $x = 0$ at 1 MHz), Figure 2. Note here we use the conventional T_m to denote the permittivity maximum associated with the relaxor-like peak and which here is associated with the onset of disorder on heating, and T^* to indicate the polar to non-polar structural transition; note that the latter is deliberately not designated as the Curie temperature, T_C, as this does not coincide with the loss of ferroelectric behaviour as defined by a switchable remanent polarisation, nor disappearance of spontaneous polarisation. A small degree of thermal hysteresis is observed (typically 10-15 K) in the low temperature anomaly (T_m); none is observed in the high temperature peak (T^*). The dielectric

losses, tan δ (Figure 2b), are dominated by the lower temperature response corresponding to the relaxor peak observed in the permittivity, Figure 2a. The degree of frequency dependence of T_m decreases with increasing x and $Ba_4Nd_{0.67}Nb_{10}O_{30}$ ($x = 1.0$) is on the cusp of normal vs relaxor behaviour and displays an incommensurate structure at room temperature as described previously.[28] The important point of note is that with increasing x, T_m increases and concomitantly T^* decreases and coalesce for $x \geq 0.75$ as summarised in Figure 2c-d. The relaxor-like peak at T_m coincides with the onset of disordering and so the low and high temperature dielectric peaks at T_m and T^* denote the limits of the disordered (but polar) region.
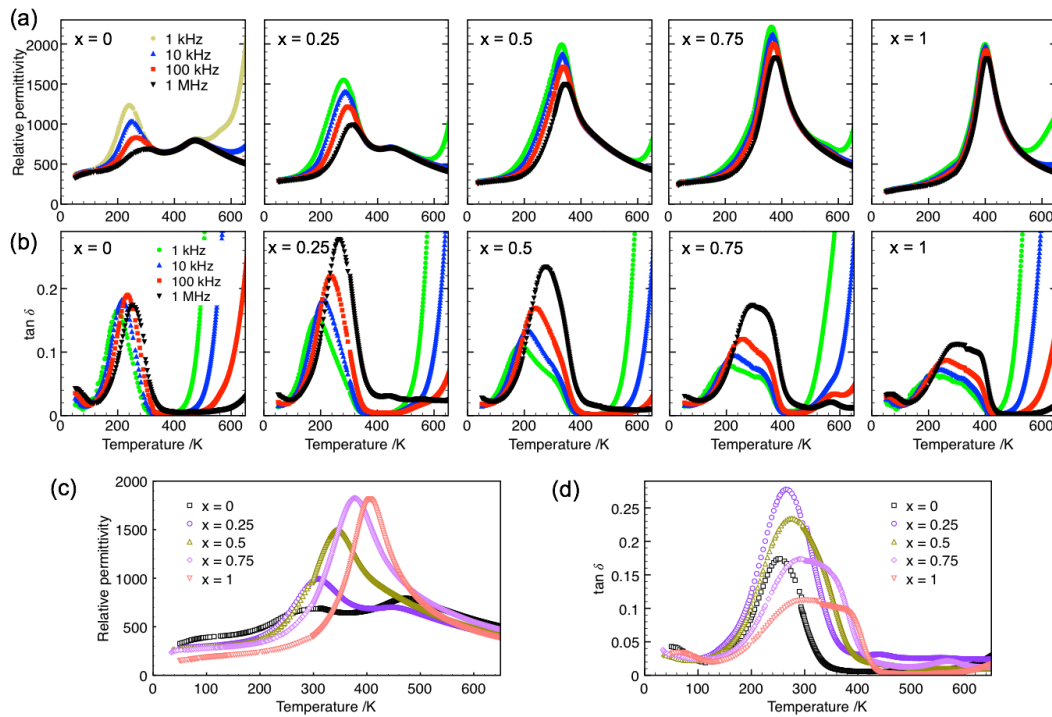

Figure 2. Relative permittivity (a) and tan δ (b) as a function of frequency and temperature for $Ba_4(La_{1-x}Nd_x)_{0.67}Nb_{10}O_{30}$ ($x = 0$, 0.25, 0.5, 0.75 and 1); comparison of permittivity (c) and loss (d) at 1 MHz.

An additional feature with small frequency dependence is observed at low temperature (< 100 K), most noticeably in the loss data, Figure 2b. Such features are quite commonly observed in low temperature dielectric data of TTBs, however the origin(s) of this common feature is not known, and several different mechanisms have been proposed for the same composition.[40, 41]

Total Neutron Scattering and Pair Distribution Function (PDF) Analysis

As a result of streaking of diffraction spots observed in selected area electron diffraction (SAED) in our previous study[28] and the hypothesis that the transition from relaxor ferroelectric to polar non-ferroelectric results from disordering of oxygen positions in the *ab*-plane, total neutron scattering was utilised to probe more closely the local structure and specifically variations in O positions as a function of temperature. Total scattering (pair distribution function, PDF) data as a function of temperature for $Ba_4La_{0.67}Nb_{10}O_{30}$ are shown in Figure 3a along with the calculated PDF generated from the crystal structure as determined from Rietveld refinement of the observed Bragg reflections at 50 K in space group *Bbm*2 as reported previously.[28] The data are in good agreement but with some subtle differences between the PDF generated from the 'Bragg structure' and the observed PDFs, particularly in the range 3-4 and 6-8 Å indicating that the 'average structure' Bragg scattering experiments are unable to detect subtle structural features that can be detected using total scattering methods. Importantly, when considering the observed PDF data, there is no obvious change associated with the relaxor ferroelectric transition around 280-300 K and which is associated with the onset of disordering. In order to probe the local structure in more detail, the observed PDF data were fitted using PDFgui.
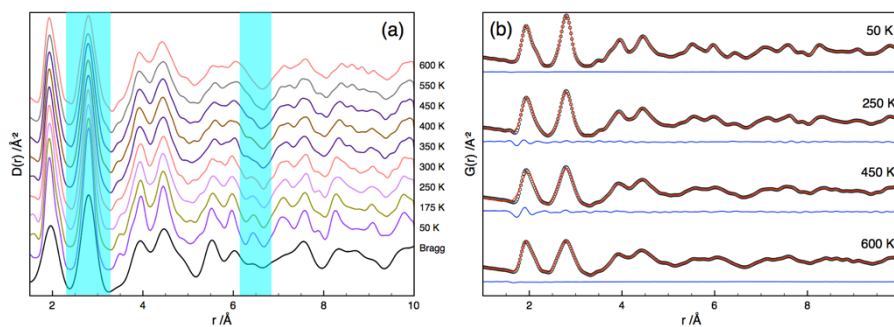

Figure 3. (a) Evolution of total scattering (PDF) data as a function of temperature. The bottom curve shows the PDF calculated from the crystal structure as determined from Rietveld refinement to the Bragg reflections at 50 K. (Data are off-set in the *y*-axis for clarity). (b) Fits to the observed data using PDFgui, refined from starting atom positions according to the crystal structures obtained by Rietveld refinement: *Bbm*2 for 50, 250 and 450 K, and *Pbam* for 600 K. (Black circles, red lines and blue lines correspond to observed data, fit and difference curves, respectively).

Several different refinement methodologies were utilised and subtle differences in the final structure were found to depend on both the order of refined parameters and also the structure used as a starting point. As the lattice parameters (determined by Rietveld refinements) should be

relatively insensitive to local disorder these were used to guide the PDF refinements, however it was noted that slight variations in lattice parameters were obtained depending on the exact starting model – full details of this methodology can be found in the SI. The lattice parameters obtained from refinement to the PDF data (with residuals, $R_w < 2.3\%$) broadly agree with the trend observed by synchrotron X-ray diffraction and, importantly, show the same change in linear thermal expansion coefficients in the 300 to 450 K range as observed by Gardner *et al.*[28] Refinement profiles of the PDF data at several selected temperatures are shown in Figure 3b. The refinement obtained at each temperature indicates an excellent fit to the data; the unit cell in each case was initially based on *Bbm*2 (50 to 450 K) and *Pbam* (550 and 600 K) structures as determined from Rietveld refinement to PND data. Note that the *Pbam* structure was used as a starting point for atom positions for 600 K, however, RUS data (discussed below) suggest that the composition is tetragonal by this point; the original assignment of the *Pbam* space group above 470 K is discussed in Refs[28, 33] and also in the SI. As the *Pbam* cell is only used for initial atom positions and all correlations due to Wyckoff multiplicity is discarded, the final outcome should be the same even if a simpler tetragonal cell was used.

To aid interpretation of the PDF data, fitting to the 50 K data was carried out using the Reverse Monte Carlo method using RMCProfile. A simple fitting procedure was adopted as the primary aim was simply to generate partial PDFs (see experimental methods for details). A1-site vacancy positions were generated at random and no site swapping was allowed as, given the small scattering contribution from La (due to the low A-site occupancy in these empty TTBs), refinement of the defect (vacancy) positions was likely to be unreliable. The resulting fit to the PDF data at 50 K is shown in Figure 4a and is in very good agreement with the data. Importantly, comparison of resulting structures and final atom positions between the RMC and PDFgui fits gave near-identical results. The individual (partial) PDFs generated from RMCProfile are shown in Figure 4b. From these (weighted) partial PDFs, $g_{ij}(r)$, it is evident that the first peak at low $r \sim 1.94$ Å corresponds to Nb-O nearest neighbour scattering the second peak at ~2.8 Å is almost entirely dominated by O-O. With increasing r, the increased mixing of partial PDFs making assignation of changes to the total PDF, $G(r)$, difficult.
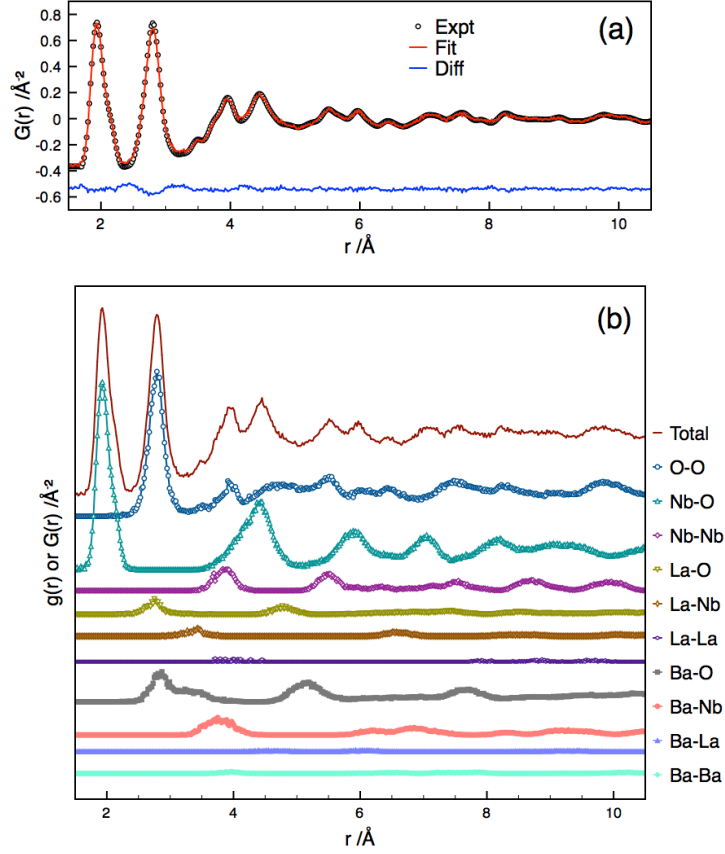
Figure 4. (a) Fit to PDF data at 50 K using RMCProfile based on a pseudo-cubic box with a $1 \times 2 \times 4$ supercell of the *Bbm*2 structure (determined by Rietveld refinement) as the starting point for atom positions. (b) Calculated weighted partial PDFs, $g_{ij}(r)$ – bottom curves, showing individual contributions to the overall total PDF, $G(r)$ – top curve.

The O-O peak at ~2.8 Å (highlighted in Figure 3a) is of interest with regard to possible O-position disorder and Figure 5a shows the temperature dependence of this peak together with the lower *r* Nb-O peak at ~1.94 Å for comparative purposes. While both peaks broaden with increasing temperature as is to be expected with a broader distribution of interatomic distances due to increased thermal motion, it is clear that the increase in O-O distribution is more significant. Each peak was fitted to a mixed Gaussian-Lorentzian function[42] in order to determine the full-width-half-maxima (FWHM) and integrated area. The integrated peak area for both remains constant indicating that the number of atoms contributing to each peak is constant over the temperature range 50 to 600 K, however, the calculated FWHM for the O-O peak at ~2.8 Å, compared to the first peak, indicates that the peak is considerably broadened with increasing temperature, and the rate of broadening increases above 270 K, Figure 5b. This broadening denotes an increase in the

distribution of O-O atomic distances, consistent with anion disorder, although the dramatic difference in temperature dependence of the Nb-O and O-O peaks, Figure 5a, may also have some contribution from correlated motion (see SI for more details). The onset of the more significant peak broadening above ~270 K is consistent with a disordering process and breakdown of Wyckoff multiplicity of the oxygen positions within the *Bbm*2 unit cell (as determined by Rietveld refinement) and, given the onset of relaxor-like behaviour observed by the macroscopic dielectric measurements, also loss of translational symmetry on longer length scales with regard to the oxygen coordinates.

From further inspection of the PDF data as a function of temperature, Figure 3a, and the weighted partial PDFs, Figure 4b, additional features at around 6.4 Å (also highlighted in Figure 3a) can also be attributed to O-O interatomic distances and which vary significantly as the temperature associated with disorder and relaxor-like behaviour (*ca.* 280 K) is approached. The evolution of this region as a function of temperature is shown in more detail in Figure 5c. At 50 K this region consists of a single broad peak but which separates into two distinct peaks by 300 K. The large unit cell and number of closely equivalent distances makes precise deconvolution of these features difficult, but examination of the structure as determined by PDF-fitting at 50 K identifies that the single peak at ~6.41 Å has contribution from axial (*c*-axis Nb-O) to equatorial (*ab*-plane Nb-O) oxygen-oxygen interatomic distances within the perovskite 'La$_{0.33}$NbO$_3$' structural units of the TTB structure, Figure 5d, and also those around the trigonal channel (see Fig S5). With increasing temperature, this peak splits into two, with peaks at ~ 6.32 Å and ~ 6.52 Å. The lower *r* peak is now dominated by the trigonal channel O-O octahedra, and the peak ~ 6.52 Å has a large contribution from O-O interatomic distances across the pentagonal, A2-cation, channel (i.e. *between* adjacent 'La$_{0.33}$NbO$_3$' units - see Fig S5). A similar peak at *ca.* 6.5 Å has been observed below T_C in SBN by Pasciak *et al.*[43] and was assigned to apical and equatorial oxygen distances in the TTB structure. The authors attributed the splitting of this peak in SBN with increasing temperature to octahedral tilting resulting in long and short O-O distances. A similar evolution is expected here, with decreased tilting on heating together with O disorder generating the significant differences in O-O distance distributions in this region.
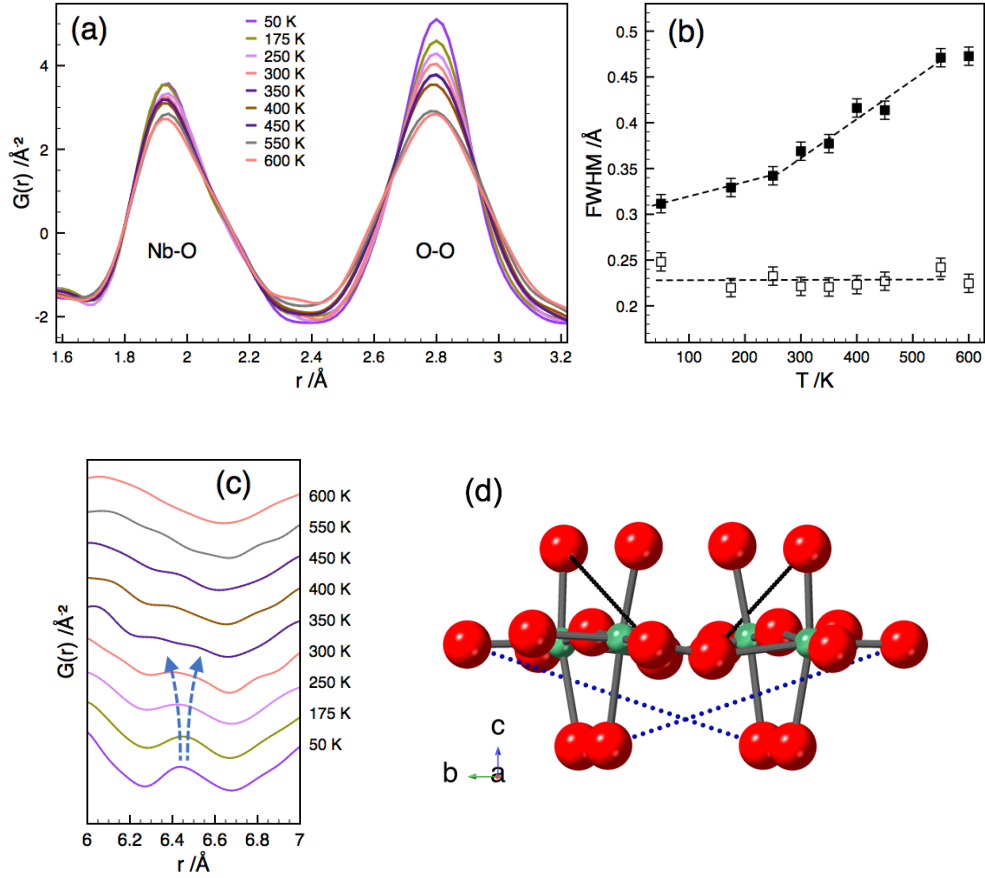
Figure 5. Temperature dependence of: (a) the low *r* peaks which are dominated by Nb-O (~1.94 Å) and O-O (~2.8 Å) nearest neighbour contributions; and (b) full-width-half-maximum (FWHM) showing broadening of the O-O peak (filled squares) in comparison to the Nb-O peak (open squares). (c) Enlarged view of the PDF data in the region 6-7 Å, indicating the change in the O-O dominated peak on heating through 300 K (associated with the onset of pinched P-E loops); (d) central perovskite unit of the TTB structure (determined from PDFgui fitting at 50 K) identifying the contribution of axial-equatorial O-O distances to the peak at *ca.* 6.4 Å (blue dotted lines indicate an O-O distance of 6.41 Å).

For $Ba_4La_{0.67}Nb_{10}O_{30}$ the change in tilting and onset of disorder on heating is self-consistent with our crystal-chemical framework model[22]. The premise of the model is that in the absence of a large driving force for tilting, either due to a small A1-cation (low tolerance factor, t_{A1}), or a sufficiently large average A-cation size to favour 'normal' displacive ferroelectricity, there is no long-range modulated tilt pattern, and relaxor behaviour results[22]. In $Ba_4La_{0.67}Nb_{10}O_{30}$, which is on the edge of the relaxor region predicted by the model, the high concentration of vacancies at the A1-site in $Ba_4La_{0.67}Nb_{10}O_{30}$ allows additional structural relaxation though O-position variation resulting in a

commensurate $\sqrt{2}a_0 \times 2\sqrt{2}b_0 \times 2c_0$ supercell (space group $Bbm2$) defined by the cation positions, but with anion disorder. The latter determine the observed relaxor behaviour.

Resonant Ultrasound Spectroscopy (RUS)

In Figure 6a, we show segments of the resonance spectra collected on the sample $Ba_4La_{0.67}Nb_{10}O_{30}$, during a cooling sequence from 1031 K (top spectrum in top panel) down to 7 K (bottom spectrum in bottom panel). From the fitting of one of these peaks, the values of f^2 and Q^{-1} are obtained (black squares in Figure 6b,c). The peak frequency values f have been normalized by the peak frequency at room temperature, f_0, for easier comparison between different samples. Both cooling and heating sequences yielded similar results.

At the highest temperature, sharp resonance peaks are observed, steadily increasing in frequency with decreasing temperature, due to normal thermal elastic stiffening. However, below 750 K, both a marked decrease in peak frequency with a minimum at $T = 528$ K and a peak broadening around this frequency minimum are observed. Although close in temperature to the dielectric anomaly for this composition (Figure 2) and which is assigned as the polar ($Bbm2$) to non-polar ($Pbam$) transition, it is evidently associated with a different transition as observed by the differing temperature dependence of this resonance peak compared to the dielectric one (see below for more discussion). The observed elastic softening associated with this resonance peak is indicative of a ferroelastic phase transition, most likely evidencing the structural transition (T_{t-o}) from the high-temperature tetragonal (t) phase (most likely $P4/mbm$) to the low temperature (also non-polar) orthorhombic (o, $Pbam$) phase. The peak in the acoustic dissipation may relate to the increase in the mobility of twin walls below the transition. Note there was no evidence of T_{t-o} during structural analysis above 500 K due to the lack of sufficient data in this range (see SI for details) and the dielectric data in this range are dominated by increasing conduction/electrode polarisation. The RUS data also show evidence of a second peak associated with the non-polar to polar transition, T^* ~470 K (this is a non-ferroelastic orthorhombic ($Pbam$) to orthorhombic ($Bbm2$) transition). Similarly there is no clear feature to distinguish the order-disorder (relaxor) transition at $T_m \sim 290$ K.

Below T_m the resonant frequency reaches a steady value, remains constant down to 80 K and then shows a progressive shift to higher values down to the lowest temperature measured (7 K), Figure 6b. In this temperature range, however, the acoustic loss shows two additional anomalies, Figure

6c: a broad peak around 264 K with a Gaussian width of 93 K, and another peak at 56 K that onsets at around 80 K. While the low temperature loss peak, together with the stiffening observed can be ascribed to a thermally activated relaxation process like the slowing down (freezing onset) of twin walls dynamics or some other microstructure, the acoustic loss around 264 K indicates the presence of a dynamic microstructure introducing dissipation in a broad range of temperatures, which is consistent with anion disorder in the structure as demonstrated by the PDF analysis described above. This disorder disrupts the long-range polar ordering,[28] leading to a polarization relaxation dynamics as evidenced both in the elasticity and dielectric measurements.
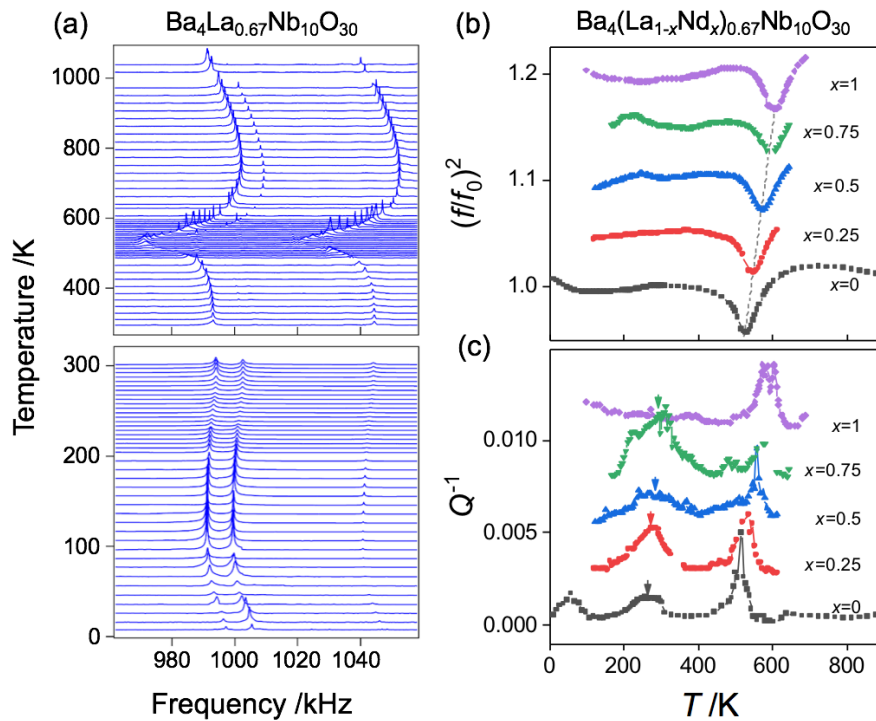

Figure 6. (a) Temperature evolution of a segment of RUS spectra corresponding to the sample with composition $Ba_4La_{0.67}Nb_{10}O_{30}$, acquired on cooling sequences in the high temperature (top) and low temperature (bottom) setups. Each spectrum has been offset up the y-axis in proportion to the temperature at which it was collected. (b) Variations with temperature of squared resonance frequencies normalized to their value at 300 K (f_0), corresponding to the fittings to selected peaks of each of the $Ba_4(La_{1-x}Nd_x)_{0.67}Nb_{10}O_{30}$ samples. The selected peaks show f_0 values of 993 kHz ($x = 0$), 728 kHz ($x = 0.25$), 494 kHz ($x = 0.5$), 762 kHz ($x = 0.75$) and 263 kHz ($x = 1$). Grey dashed line is a guide to the eye. (c) Temperature evolution of the Q^{-1} values obtained from the same fittings, arrows indicate peak temperature from Gaussian fittings to loss peaks associated with the relaxor peak (T_m) observed in the dielectric data. Plots in (b,c) are shifted vertically for clarity.

RUS measurements for the sample with Nd fully substituting La in the A1 site ($Ba_4Nd_{0.67}Nb_{10}O_{30}$, $x = 1$) display a similar temperature dependence of f^2 and Q^{-1} (purple diamonds – top data set – in Figure 6b,c) with two main differences: a) both T_{t-o} and the freezing onset are shifted to higher temperatures ($T_{t-o} = 607$ K and freezing onset ~ 150 K); and b) no loss peak between these two temperatures is observed, thus evidencing the suppression of disorder in this composition, in accordance with the recovery of normal ferroelectric behaviour.

For comparison, samples with intermediate compositions $Ba_4(La_{1-x}Nd_x)_{0.67}Nb_{10}O_{30}$ (with $x = 0.25$, 0.5 and 0.75) were also measured in the RUS setups between 650 and 120 K. From the temperature dependence of f^2 and Q^{-1} from selected resonance peaks for each sample, it is observed that T_{t-o} displays a linear dependence with x, Figure 7, showing that an orthorhombic distortion becomes progressively more stable with increasing Nd content which is to be expected given the decreasing average A-cation size and increased octahedral tilting in the structure. As mentioned above, the compositional dependence of this peak in RUS also confirms that this peak is not associated with the dielectric anomaly at T^*, which, by contrast, moves to lower temperature with increasing x, Figure 7. The clarity of this high temperature feature highlights RUS as a complementary technique for study of structural evolution of materials due to the sensitivity of elastic constants to structural transitions.

The peak in the acoustic loss at near-ambient temperatures is observed for all compositions with $x \leq 1$, consistent with T_m as observed in other relaxor TTBs[44]. The loss peak temperature also displays a composition dependence (indicated by arrows in Figure 6c), shifting to higher temperatures as x is increased. This behaviour is again consistent with the dielectric data which show an increase in the temperature of the dielectric anomaly (T_m) associated with the disordering process with increasing x.
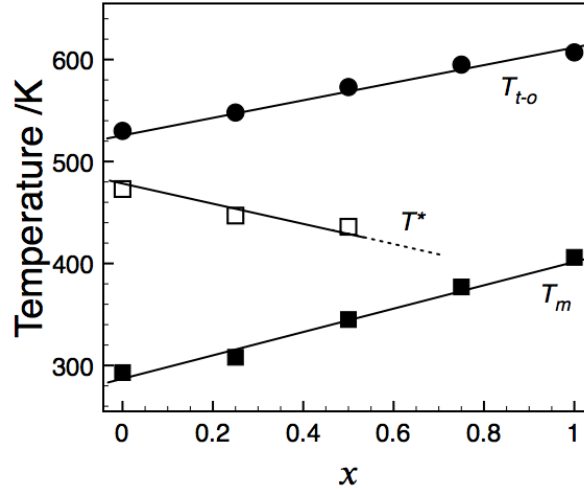
Figure 7. Variation in transition temperatures as a function x in $Ba_4(La_{1-x}Nd_x)_{0.67}Nb_{10}O_{30}$; T_m and T^* denote the order-disorder and polar to non-polar transition temperatures as determined from the maxima in dielectric permittivity (at 1 MHz, Figure 2a); T_{t-o} denotes the suggested transition from the high temperature tetragonal (t) to orthorhombic (o) phase as determined from RUS data (Figure 6b). Curves are provided only as a guide to the eye.

Summary and Conclusions

The pair distribution function (PDF) data obtained from total neutron scattering for the empty TTB composition $Ba_4La_{0.67}Nb_{10}O_{30}$ shows subtle differences from that generated from the average structure as determined from Rietveld refinements. Specifically, variable temperature PDF analysis shows a clear change in the O-O distance distribution above *ca.* 270 K as denoted by the change in gradient of the FWHM *vs* temperature data; this change would not generally be expected from increased thermal motion. The increase is consistent with the proposed anion disorder associated with the relaxor behaviour and loss of remanent polarisation observed at *ca.* 270 K observed in the electrical response. The PDF data also indicate a change in tilting behaviour of the 'La_{0.33}NbO_3' perovskite units in the TTB structure at the order-disorder transition; a bifurcation of the PDF peak at *ca.* 6.4 Å indicates a reduction in the degree of tilting. Resonant ultrasound spectroscopy (RUS) data are consistent with the observed structural behaviour: there is no observed change in the resonant frequency at the order-disorder transition consistent with the lack of change in symmetry, however, the mechanical loss is clearly sensitive to the anion disorder, showing a peak at T_m, as is to be expected with an increase in anharmonicity due to the increase in

distribution of local O^{2-} environments. In terms of the crystal-chemical framework model for TTBs which rationalises relaxor *vs.* 'normal' ferroelectric behaviour, this empty TTB composition is expected to exhibit an incommensurate structure and relaxor behaviour when compared to the filled composition $Ba_4La_2Ti_4Nb_6O_{30}$, however the combination of reduced tilting in the presence of significant A-site vacancies allows structural relaxation of any frustrated tilt modulation *via* anion disorder. In the absence of a propagating (modulated) tilt system $Ba_4La_{0.67}Nb_{10}O_{30}$ therefore has a commensurate structure but nevertheless exhibits relaxor behaviour; the anion disorder also disrupts the long-range polar ordering giving rise to the collapse of macroscopic polarisation.

RUS data for the series $Ba_4(La_{1-x}Nd_x)_{0.67}Nb_{10}O_{30}$ indicate a clear increase in the order-disorder transition temperature (T_m) with increasing x in line with the dielectric data and consistent with the crystal-chemical framework model where the reduced A1-cation size (decreasing t_{A1}) increases the degree of octahedra tilting and delays the onset of disordering. The polar to non-polar transition (T^*) is not easily identified by RUS, however the data clearly show a higher temperature transition presumably to the tetragonal aristotype phase and which increases in temperature with increasing x.

In summary both variable temperature PDF and RUS analysis support the proposed origin of relaxor behaviour as an anion order-disorder transition in the empty TTB series $Ba_4(La_{1-x}Nd_x)_{0.67}Nb_{10}O_{30}$. This disordering process is responsible for relaxor behaviour and loss of macroscopic (long-range) polarisation. Reducing the A1 cation size suppresses disordering by inducing a greater degree of tilting.

Supporting Information

Details of structural analysis procedures using (neutron) total scattering data; summary of lattice parameters; supporting structural analysis at high temperature using synchrotron and neutron powder diffraction.

Acknowledgements

References

1. Dickens, P. G.; Whittingham, M. S., The tungsten bronzes and related compounds. *Quarterly Reviews, Chemical Society* **1968,** 22, (1), 30.

2. Francombe, M. H., The relation between structure and ferroelectricity in lead barium and barium strontium niobates. *Acta Crystallographica* **1960,** 13, (2), 131-140.

3. Jamieson, P. B.; Abrahams, S. C.; Bernstein, J. L., Ferroelectric Tungsten Bronze-Type Crystal Structures. I. Barium Strontium Niobate $Ba_{0.27}Sr_{0.75}Nb_2O_{5.78}$. *The Journal of Chemical Physics* **1968,** 48, (11), 5048-5057.

4. Jamieson, P. B.; Abrahams, S. C.; Bernstein, J. L., Ferroelectric Tungsten Bronze-Type Crystal Structures. II. Barium Sodium Niobate $Ba_{(4+x)}Na_{(2-2x)}Nb_{10}O_{30}$. *The Journal of Chemical Physics* **1969,** 50, (10), 4352-4363.

5. Bursill, L. A.; Lin, P. J., Incommensurate superstructures and phase transition of strontium barium niobate (SBN). *Acta Crystallographica Section B Structural Science* **1987,** 43, (1), 49-56.

6. Chu, F.; Setter, N.; Tagantsev, A. K., The spontaneous relaxor-ferroelectric transition of $Pb(Sc_{0.5}Ta_{0.5})O_3$. *J Appl Phys* **1993,** 74, (8), 5129-5134.

7. Fu, D.; Taniguchi, H.; Itoh, M.; Koshihara, S. Y.; Yamamoto, N.; Mori, S., Relaxor $Pb(Mg_{(1/3)}Nb_{(2/3)})O_3$: a ferroelectric with multiple inhomogeneities. *Phys Rev Lett* **2009,** 103, (20), 207601.

8. Viehland, D.; Jang, S. J.; Cross, L. E.; Wuttig, M., Deviation from Curie-Weiss behavior in relaxor ferroelectrics. *Phys Rev B Condens Matter* **1992,** 46, (13), 8003-8006.

9. Levin, I.; Reaney, I. M., Nano- and Mesoscale Structure of $Na_{1/2}Bi_{1/2}TiO_3$: A TEM Perspective. *Advanced Functional Materials* **2012,** 22, (16), 3445-3452.

10. Levin, I.; Reaney, I. M.; Anton, E. M.; Jo, W.; Rödel, J.; Pokorny, J.; Schmitt, L. A.; Kleebe, H. J.; Hinterstein, M.; Jones, J. L., Local structure, pseudosymmetry, and phase transitions in $Na_{1/2}Bi_{1/2}TiO_3$–$K_{1/2}Bi_{1/2}TiO_3$ ceramics. *Physical Review B* **2013,** 87, (2).

11. Neagu, A.; Tai, C.-W., Local disorder in $Na_{0.5}Bi_{0.5}TiO_3$ - piezoceramic determined by 3D electron diffuse scattering. *Scientific Reports* **2017,** 7, (1).

12. Levin, I.; Keeble, D. S.; Cibin, G.; Playford, H. Y.; Eremenko, M.; Krayzman, V.; Laws, W. J.; Reaney, I. M., Nanoscale Polar Heterogeneities and Branching Bi-Displacement Directions in $K_{0.5}Bi_{0.5}TiO_3$. *Chemistry of Materials* **2019,** 31, (7), 2450-2458.

13. Li, F.; Zhang, S.; Damjanovic, D.; Chen, L.-Q.; Shrout, T. R., Local Structural Heterogeneity and Electromechanical Responses of Ferroelectrics: Learning from Relaxor Ferroelectrics. *Advanced Functional Materials* **2018,** 28, (37).

14. Jiang, B.; Raeder, T. M.; Lin, D.-Y.; Grande, T.; Selbach, S. M., Structural Disorder and Coherence across the Phase Transitions of Lead-Free Piezoelectric $Bi_{0.5}K_{0.5}TiO_3$. *Chemistry of Materials* **2018,** 30, (8), 2631-2640.

15.   Glass, A. M., Investigation of the Electrical Properties of $Sr_{1-x}Ba_xNb_2O_6$ with Special Reference to Pyroelectric Detection. *J Appl Phys* **1969,** 40, (12), 4699-4713.

16.   Lines, M. E.; Glass, A. M., *Principles and applications of ferroelectrics and related materials*. Clarendon Press: Oxford Eng., 1977; p xiii, 680 p.

17.   Kirk, C. A.; Stennett, M. C.; Reaney, I. M.; West, A. R., A new relaxor ferroelectric, $Ba_2LaTi_2Nb_3O_{15}$. *Journal of Materials Chemistry* **2002,** 12, (9), 2609-2611.

18.   Miles, G. C.; Stennett, M. C.; Pickthall, D.; Kirk, C. A.; Reaney, I. M.; West, A. R., X-ray diffraction data for the new ferroelectric tetragonal tungsten bronze phases, $Ba_2RETi_2M_3O_{15}$: M = Nb and RE = La, Pr, Nd, Sm, Gd, Dy, (Bi); M = Ta and RE = La, Nd. *Powder Diffraction* **2012,** 20, (1), 43-46.

19.   Miles, G. C.; Stennett, M. C.; Reaney, I. M.; West, A. R., Temperature-dependent crystal structure of ferroelectric $Ba_2LaTi_2Nb_3O_{15}$. *Journal of Materials Chemistry* **2005,** 15, (7), 798.

20.   Levin, I.; Stennett, M. C.; Miles, G. C.; Woodward, D. I.; West, A. R.; Reaney, I. M., Coupling between octahedral tilting and ferroelectric order in tetragonal tungsten bronze-structured dielectrics. *Appl Phys Lett* **2006,** 89, (12), 122908.

21.   Stennett, M. C.; Reaney, I. M.; Miles, G. C.; Woodward, D. I.; West, A. R.; Kirk, C. A.; Levin, I., Dielectric and structural studies of $Ba_2MTi_2Nb_3O_{15}$ ($BMTNO_{15}$, $M=Bi^{3+},La^{3+},Nd^{3+},Sm^{3+},Gd^{3+}$) tetragonal tungsten bronze-structured ceramics. *J Appl Phys* **2007,** 101, (10), 104114.

22.   Zhu, X.; Fu, M.; Stennett, M. C.; Vilarinho, P. M.; Levin, I.; Randall, C. A.; Gardner, J.; Morrison, F. D.; Reaney, I. M., A Crystal-Chemical Framework for Relaxor versus Normal Ferroelectric Behavior in Tetragonal Tungsten Bronzes. *Chemistry of Materials* **2015,** 27, (9), 3250-3261.

23.   Huang, C. J.; Li, K.; Liu, X. Q.; Zhu, X. L.; Chen, X. M.; Johnson, D., Effects of A1/A2-Sites Occupancy upon Ferroelectric Transition in $(Sr_xBa_{1-x})Nb_2O_6$ Tungsten Bronze Ceramics. *J Am Ceram Soc* **2014,** 97, (2), 507-512.

24.   Zhu, X. L.; Wu, S. Y.; Chen, X. M., Dielectric anomalies in $(Ba_xSr_{1-x})_4Nd_2Ti_4Nb_6O_{30}$ ceramics with various radius differences between A1- and A2-site ions. *Appl Phys Lett* **2007,** 91, (16), 162906-3.

25.   Zhu, X. L.; Li, K.; Chen, X. M., Ferroelectric Transition and Low-Temperature Dielectric Relaxations in Filled Tungsten Bronzes. *J Am Ceram Soc* **2014,** 97, (2), 329-338.

26.   Josse, M.; Heijboer, P.; Albino, M.; Molinari, F.; Porcher, F.; Decourt, R.; Michau, D.; Lebraud, E.; Veber, P.; Velazquez, M.; Maglione, M., Original Crystal-Chemical Behaviors in $(Ba,Sr)_2Ln(Fe,Nb,Ta)_5O_{15}$ Tetragonal Tungsten Bronze: Anion-Driven Properties Evidenced by Cationic Substitutions. *Crystal Growth & Design* **2014,** 14, (11), 5428-5435.

27.   Kinka, M.; Gabrielaitis, D.; Albino, M.; Josse, M.; Palaimiene, E.; Grigalaitis, R.; Maglione, M.; Banys, J., Investigation of Dielectric Relaxation Processes in $Ba_2NdFeNb_{4-x}Ta_xO_{15}$ Ceramics. *Ferroelectrics* **2015,** 485, (1), 101-109.

28.   Gardner, J.; Yu, F.; Tang, C.; Kockelmann, W.; Zhou, W.; Morrison, F. D., Relaxor-to-Ferroelectric Crossover and Disruption of Polar Order in "Empty" Tetragonal Tungsten Bronzes. *Chemistry of Materials* **2016,** 28, (13), 4616-4627.

29.   Gardner, J.; Morrison, F. D., A-site size effect in a family of unfilled ferroelectric tetragonal tungsten bronzes: $Ba_4R_{0.67}Nb_{10}O_{30}$ (R = La, Nd, Sm, Gd, Dy and Y). *Dalton transactions* **2014,** 43, (30), 11687-95.

30.   Gardner, J.; Morrison, F. D., Manipulation of polar order in the "empty" tetragonal tungsten bronzes: $Ba_{4-x}Sr_xDy_{0.67}\square_{1.33}Nb_{10}O_{30}$, x = 0, 0.25, 0.5, 1, 2, 3. *Appl Phys Lett* **2016,** 109, (7).

31.   Li, K.; Zhu, X. L.; Liu, X. Q.; Ma, X.; Sen Fu, M.; Kroupa, J.; Kamba, S.; Chen, X. M., Electric-field-induced phase transition and pinched P–E hysteresis loops in Pb-free ferroelectrics with a tungsten bronze structure. *NPG Asia Materials* **2018,** 10, (4), 71-81.

32.   Li, C.; Hong, J. S.; Huang, Y. H.; Ma, X.; Fu, M. S.; Li, J.; Liu, X. Q.; Wu, Y. J., Pinched P-E hysteresis loops in $Ba_4Sm_2Fe_{0.5}Ti_3Nb_{6.5}O_{30}$ ceramic with tungsten bronze structure. *Appl Phys Lett* **2019,** 115, (8).

33.   Gardner, J. Ferroelectricity in empty tetragonal tungsten bronzes. PhD, University of St Andrews, 2017.

34.   Larson, A. C.; Von Dreele, R. B. *General Structure Analysis System (GSAS)*; 1994; p 86.

35.   Farrow, C. L.; Juhas, P.; Liu, J. W.; Bryndin, D.; Bozin, E. S.; Bloch, J.; Proffen, T.; Billinge, S. J., PDFfit2 and PDFgui: computer programs for studying nanostructure in crystals. *J Phys Condens Matter* **2007,** 19, (33), 335219.

36.   McGreevy, R. L., Reverse Monte Carlo modelling. *Journal of Physics: Condensed Matter* **2001,** 13, (46), R877-R913.

37.   McKnight, R. E. A.; Carpenter, M. A.; Darling, T. W.; Buckley, A.; Taylor, P. A., Acoustic dissipation associated with phase transitions in lawsonite, $CaAl_2Si_2O_7(OH)_2 \cdot H_2O$. *American Mineralogist* **2007,** 92, (10), 1665-1672.

38.   McKnight, R. E. A.; Moxon, T.; Buckley, A.; Taylor, P. A.; Darling, T. W.; Carpenter, M. A., Grain size dependence of elastic anomalies accompanying the α–β phase transition in polycrystalline quartz. *Journal of Physics: Condensed Matter* **2008,** 20, (7).

39.   Migliori, A.; Maynard, J. D., Implementation of a modern resonant ultrasound spectroscopy system for the measurement of the elastic moduli of small solid specimens. *Review of Scientific Instruments* **2005,** 76, (12).

40.   Ko, J.-H.; Kojima, S.; Lushnikov, S. G.; Katiyar, R. S.; Kim, T.-H.; Ro, J.-H., Low-temperature transverse dielectric and pyroelectric anomalies of uniaxial tungsten bronze crystals. *J Appl Phys* **2002,** 92, (3), 1536-1543.

41.   Xu, Y.; Li, Z.; Li, W.; Wang, H.; Chen, H., Phase transition of some ferroelectric niobate crystals with tungsten-bronze structure at low temperatures. *Phys Rev B Condens Matter* **1989,** 40, (17), 11902-11908.

42.   Ansell, R. O.; Dickinson, T.; Povey, A. F.; Sherwood, P. M. A., X-ray photoelectron spectroscopic studies of electrode surfaces using a new controlled transfer technique. *Journal of Electroanalytical Chemistry and Interfacial Electrochemistry* **1979,** 98, (1), 79-89.

43.   Paściak, M.; Ondrejkovic, P.; Kulda, J.; Vaněk, P.; Drahokoupil, J.; Steciuk, G.; Palatinus, L.; Welberry, T. R.; Fischer, H. E.; Hlinka, J.; Buixaderas, E., Local structure of relaxor ferroelectric $Sr_xBa_{1-x}Nb_2O_6$ from a pair distribution function analysis. *Physical Review B* **2019,** 99, (10).

44.   Rotaru, A.; Schiemer, J. A.; Carpenter, M. A., Elastic and anelastic relaxations accompanying relaxor ferroelectric behaviour of $Ba_6GaNb_9O_{30}$ tetragonal tungsten bronze from resonant ultrasound spectroscopy. *Journal of Thermal Analysis and Calorimetry* **2016,** 124, (2), 571-583.

Table of contents graphic